

Article

Manipulating Transverse Spin Angular Momentum with Symmetrically Modulated Hybridly Polarized Vector Optical Field

Xue-Feng Sun, Yue Pan, Guang-Bo Zhang, Zhong-Xiao Man and Xu-Zhen Gao *

School of Physics and Physical Engineering, Shandong Provincial Key Laboratory of Laser Polarization and Information Technology, Qufu Normal University, Qufu 273165, China

* Correspondence: xzhgao@qfnu.edu.cn

Abstract: Transverse spin angular momentum (SAM) of photon, also known as ‘photonic wheel’, has attracted much attention, owing to its extraordinary properties and broad application prospect. Thus, it is essential to flexibly manipulate the transverse SAM in order to satisfy different needs. In this article, we design and generate a new kind of symmetrically modulated hybridly polarized vector optical field (SM-HP-VOF), and pure transverse SAM can be achieved based on the tightly focused SM-HP-VOF. Through adjusting the parameters of the SM-HP-VOF, the shape, intensity, and symmetry of the transverse SAM can be modulated. Moreover, by adding a segmented vortex phase distribution to the SM-HP-VOF, the transverse SAM becomes more concentrated and stronger, indicating that the orbital angular momentum can be a catalyst in modulating transverse SAM. Such results can provide a new avenue in studying and modulating transverse SAM, which would have potential applications in various areas including chip optical circuitry, optical quantum computing, and optical trapping and manipulation.

Keywords: transverse spin angular momentum; vector optical field; symmetry; orbital angular momentum



Citation: Sun, X.-F.; Pan, Y.; Zhang, G.-B.; Man, Z.-X.; Gao, X.-Z. Manipulating Transverse Spin Angular Momentum with Symmetrically Modulated Hybridly Polarized Vector Optical Field. *Photonics* **2022**, *9*, 817. <https://doi.org/10.3390/photonics9110817>

Received: 13 October 2022

Accepted: 28 October 2022

Published: 29 October 2022

Publisher’s Note: MDPI stays neutral with regard to jurisdictional claims in published maps and institutional affiliations.



Copyright: © 2022 by the authors. Licensee MDPI, Basel, Switzerland. This article is an open access article distributed under the terms and conditions of the Creative Commons Attribution (CC BY) license (<https://creativecommons.org/licenses/by/4.0/>).

1. Introduction

In recent years, manipulation of polarization has become an appealing and promising topic of physical optics, due to its important role in engineering optical fields and light–matter interaction. As a representative example of manipulating polarization, vector optical field (VOF) with space-variant polarization distribution on the wave front has a growing interest [1,2], owing to the novel optical effects and wide applications such as optical trapping [3,4], focal engineering [5–8], quantum entanglement [9,10], optical microscopy [11,12], and optical communications [13–15]. Among various VOFs, the hybridly polarized vector optical field (HP-VOF), which comprises the linear, elliptic, and circular polarizations in the wavefront of the field simultaneously, attracts great attention [16–22].

As is well known, light can carry both spin angular momentum (SAM) and orbital angular momentum (OAM), which are related to the polarization and phase of light, respectively. The SAM is associated with the circular polarizations with two possible quantized values of $\pm\hbar$, which can make the particle spin around its own axis. The conventional SAM is called the longitudinal SAM, which is parallel or antiparallel to the propagation direction of the optical field. The longitudinal SAM corresponds to the two-dimensional polarization, which will be limited when studying the electric field with three spatial components in special conditions. Thus, in addition to the longitudinal SAM, there must be a kind of transverse SAM. The transverse SAM, whose spin vector is perpendicular to the propagating direction, has attracted extensive attention [23–39]. As the VOF and transverse SAM density are both related to the polarization of light, it is promising to use the VOF in manipulating SAM [25,27–30,32,33,36,37,39–45].

In this paper, we propose a new kind of symmetrically modulated hybridly polarized vector optical field (SM-HP-VOF), and the pure longitudinal SAM in the input plane can transform into pure transverse SAM in the focal plane. With the flexibly modulated SM-HP-VOF, the feature of the transverse SAM can be manipulated. We further add a segmented vortex phase distribution to the wave front of the SM-HP-VOF, in order to concentrate and enhance the transverse SAM. This means the OAM of light can also affect the distribution of the transverse SAM. Such results can be exploited in various areas needing flexibly modulated SAM.

2. Design and Generation of SM-HP-VOF

To design the SM-HP-VOF, we divided the circular wave front of the optical field into $2N$ congruent sectors, and the range of the n -th sector is:

$$\varphi_{n-1} \leq \varphi < \varphi_n, n = 1, 2, \dots, 2N, \tag{1}$$

where φ is the azimuthal coordinate on the wave front, and $\varphi_n = n\pi/N$ is the azimuthal coordinate of the boundary between the n -th and $(n + 1)$ -th sector.

The first sector is filled with the traditional cylindrical HP-VOF, which is based on the expression of the polarization state on Poincaré sphere [16,17]. The expression of optical field in the first sector is:

$$\mathbf{E}_1(\varphi) = \sin\left(m\varphi + \frac{\pi}{4}\right)e^{-i\phi_1}\hat{\mathbf{e}}_r + \cos\left(m\varphi + \frac{\pi}{4}\right)e^{-i\phi_1}\hat{\mathbf{e}}_l; 0 \leq \varphi < \varphi_1 \tag{2}$$

where m is the topological charge of the cylindrical HP-VOF in the first sector, and $\hat{\mathbf{e}}_r = (\hat{\mathbf{e}}_x + i\hat{\mathbf{e}}_y)/\sqrt{2}$ and $\hat{\mathbf{e}}_l = (\hat{\mathbf{e}}_x - i\hat{\mathbf{e}}_y)/\sqrt{2}$ are right-handed and left-handed circular polarization basis vectors. The orientation of the polarization on the wave front is ϕ_1 with respect to the x axis, and $2\phi_1$ corresponds to the longitude coordinate on the Poincaré sphere representing the polarization. The ellipticity of polarization is controlled by $\alpha_1 = m\varphi$, and $2\alpha_1$ corresponds to the latitude coordinate on the Poincaré sphere. The ellipticity of polarization is $\tan \alpha_1$.

For the optical field above the x axis when $1 \leq n \leq N$, we designed the polarization state of the optical field based on the symmetry principle, and the optical field in n -th sector is symmetric with the $(n - 1)$ -th optical field. Here, we continued to use the longitude and latitude coordinates on the Poincaré sphere to represent the polarization state of the optical field. The polarization state of the optical field in the n -th sector can be represented by the coordinates on the Poincaré sphere $(2\phi_n, 2\alpha_n)$. The recursive formula of ϕ_n and α_n for the polarization state of the optical field in the n -th sector is:

$$\phi_n = 2\phi_{n-1} - \phi_{n-1}, \tag{3}$$

$$\alpha_n = \text{mod}(n - 1, 2)m\frac{2\pi}{N} - \alpha_{n-1}, \tag{4}$$

where $n = 2, 3, 4 \dots N$. $\text{mod}(a, b)$ is the remainder of a/b . In this article, we take $\phi_1 = 0$ and $\alpha_1 = m\varphi$ corresponding to the cylindrical HP-VOF in the first sector. The orientation of polarization ϕ_n is based on ϕ_{n-1} , and the orientation is symmetric about the axis of $\varphi = \varphi_{n-1}$. The ellipticity of polarization is determined by α_n . When $n = 1$, α_1 increases from 0 to $m\varphi_1$ as φ increases. When n is odd, $\alpha_n = m[\varphi - (n - 1)\pi/N]$, $\varphi_{n-1} \leq \varphi < \varphi_n$. The range of $[\varphi - (n - 1)\pi/N]$ is $[0, \pi/N)$, which means that the change of α_n is completely equivalent to the change of α_1 . In addition, when n is even, $\alpha_n = m[n\pi/N - \varphi]$, $\varphi_{n-1} \leq \varphi < \varphi_n$. The range of $[n\pi/N - \varphi]$ is $[\pi/N, 0)$, which means that the change of α_n is completely opposite to the change of α_1 . This can guarantee the symmetry of the ellipticity of polarization. Based on the Poincaré sphere, the expression for the optical field in the n -th sector is:

$$\mathbf{E}_n(\varphi) = \sin\left(\alpha_n + \frac{\pi}{4}\right)e^{-i\varphi_n}\hat{\mathbf{e}}_r + \cos\left(\alpha_n + \frac{\pi}{4}\right)e^{i\varphi_n}\hat{\mathbf{e}}_l; \varphi_{n-1} \leq \varphi < \varphi_n, n = 1, 2, 3, \dots, N. \tag{5}$$

For the optical field below the x axis when $N + 1 \leq n \leq 2N$, the optical fields in the n -th and $(n - N)$ -th sectors are the complex conjugate of each other. In this way, the optical fields at the central symmetric positions have conjugate symmetry. Then the expression of the optical field in the n -th sector is:

$$\mathbf{E}_n(\varphi) = \left[\sin\left(\alpha_n + \frac{\pi}{4}\right)e^{-i\varphi_n}\hat{\mathbf{e}}_r + \cos\left(\alpha_n + \frac{\pi}{4}\right)e^{i\varphi_n}\hat{\mathbf{e}}_l \right]^*, \varphi_{n-1} \leq \varphi < \varphi_n, n = N + 1, N + 2 \dots 2N. \tag{6}$$

Therefore, the SM-HP-VOF can be expressed as:

$$\mathbf{E}(\varphi) = \sum_{n=1}^{2N} \mathbf{E}_n(\varphi). \tag{7}$$

In order to generate the SM-HP-VOF, we performed the experiment using a 4f system and spatial light modulator (SLM), which is a universal method for generating VOFs [4,16,46]. The input horizontal polarized beam is incident on the SLM and is divided to ± 1 st orders. The two orders are allowed to pass through a spatial filter and then are converted into two orthogonally $\pm 45^\circ$ linearly polarized fields by a pair of half-wave plates. The two orthogonally linearly polarized parts are recombined by the Ronchi phase grating placed in the output plane of the 4f system. We should point out that the innovation of this paper is that we achieved the above designed SM-HP-VOF, and this experimental method is a common method to generate VOFs. In Figure 1, the first row shows the simulated polarization state and the normalized Stokes parameters of the SM-HP-VOF when $(N, m) = (2, 1)$ in Equations (2)–(7), and the second row presents the corresponding experimental results. In the experimentally measured total intensity pattern, there occur two black singular lines, which originate from the π phase difference beside the lines. It can be seen that the polarizations in the sector when $n = 1$ and 2 are right-handed elliptic (circular) polarizations, while the polarizations in the sector when $n = 3$ and 4 are left-handed elliptic (circular) polarizations. Clearly, the experimental results are in good agreement with the simulated ones, but it was still found that the measured Stokes parameter S_2 was slightly different from the theoretical result, and the error was caused by the quarter-wave retarder plate and polarizer in the experiment.

Figure 2 shows the simulated and generated SM-HP-VOFs when $(N, m) = (2, 2)$ and $(4, 2)$, respectively. The first and third rows show the simulated polarization states and normalized Stokes parameters of the SM-HP-VOF, and the second and fourth rows present the experimental results. Singular lines can also be found in the experimentally measured total intensity patterns, and the black singular lines on x and y axes when $(N, m) = (2, 2)$ also originated from the phase difference of π . For the SM-HP-VOF when $(N, m) = (4, 2)$, there are two kinds of singular lines. The black singular line on the x axis is also due to the phase difference of π , leading to the complete extinction of light on the singular line. Meanwhile, the other two singular lines exhibit partial extinction. This phenomenon is because the polarizations beside the singular line are vertically and horizontally polarized, respectively. When $(N, m) = (2, 2)$, the polarization changing speed is two times of the case when $(N, m) = (2, 1)$ in Figure 1. This is easy to understand as the topological charge m can control the changing period of the polarization in the cylindrical HP-VOF. When $(N, m) = (4, 2)$, there are 8 sectors to modulate the polarization state of the SM-HP-VOF, and the polarizations above x axis are right-handed elliptic (circular) polarizations, while the polarizations below x axis are left-handed elliptic (circular) polarizations. The experimental results are in good agreement with the simulated ones.

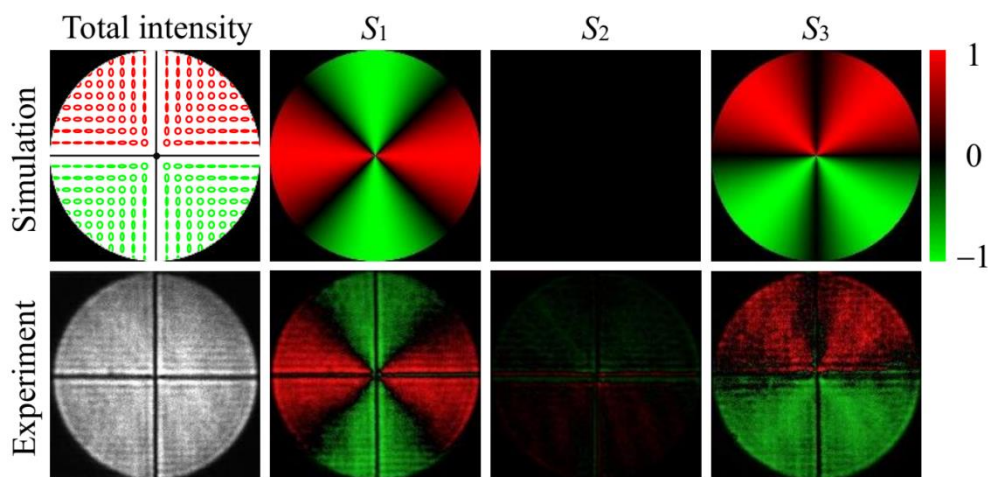


Figure 1. Simulated and measured SM-HP-VOF when $(N, m) = (2, 1)$. The first and second rows show the simulated and experimental results of the SM-HP-VOF. The first column shows the polarization state and the experimental total intensity pattern. The red and green polarizations represent right- and left-handed elliptic (circular) polarizations, respectively. Stokes parameters S_1 , S_2 , and S_3 are given in the second to fourth columns, respectively.

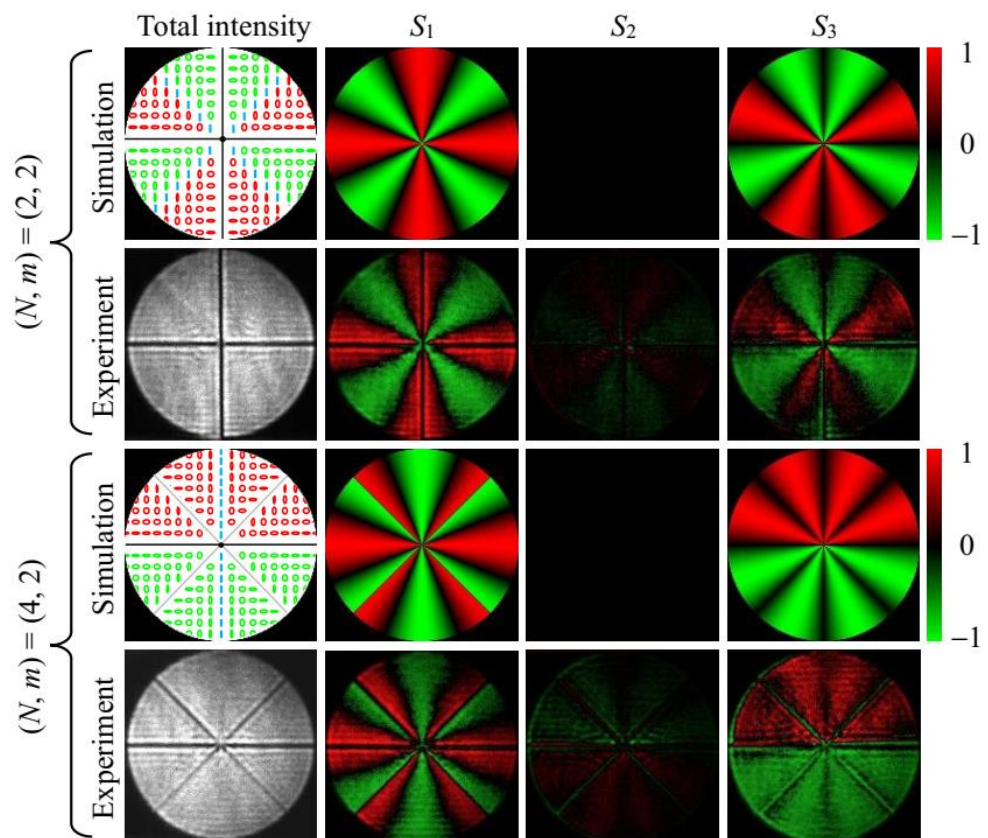


Figure 2. Simulated and measured SM-HP-VOF. The first and second rows correspond to the case when $(N, m) = (2, 2)$, and the third and fourth rows correspond to the case when $(N, m) = (4, 2)$. The first and third rows show the simulated results of the SM-HP-VOF, and the second and fourth rows show the corresponding experimental results. The first column shows the polarization states and the experimental total intensity patterns. The blue, red, and green polarizations represent linear, right- and left-handed elliptic (circular) polarizations, respectively. Stokes parameters S_1 , S_2 , and S_3 are given in the second to fourth columns, respectively.

3. The Manipulation of the Transverse SAM of the Tightly Focused SM-HP-VOF

As we have introduced, SAM density is an essential property of light, and the achievement of the transverse SAM density is important due to its various applications [23–39]. When calculating the three-dimensional SAM density, the transverse SAM density S_t is the superposition of x - and y -components of the SAM density as $S_t = \sqrt{S_x + S_y}$. To achieve transverse SAM density, it is natural to think of the tightly focused field, which may have a nonzero longitudinal component. Now we will study the tightly focused SM-HP-VOF based on a lens with numerical aperture $NA = 0.95$, and further discuss the transverse SAM density of SM-HP-VOF. According to the Richards–Wolf vectorial diffraction theory [47,48] and formula of the time-averaged SAM density [24,31,40,49–51], we can calculate the tightly focused field and the SAM density distribution in the focal plane.

Figure 3 shows the SAM density of the tightly focused HP-VOF and SM-HP-VOF. The first column shows the polarization states of the VOFs in the input plane. We can see that the most prominent difference between the SM-HP-VOF and the conventional cylindrical HP-VOF is that the polarizations of the SM-HP-VOF at the central symmetric positions are with opposite SAM, while the SAM is the same for the case of the HP-VOF. This difference is due to the fact that the electric fields at the central symmetric positions are the complex conjugate of each other for the SM-HP-VOF, as shown in Equation (6). For the cylindrical HP-VOF when $m = 1$, there is one focal spot in the focal plane, and both transverse and longitudinal SAM density appear in the focal plane. For the SM-HP-VOF, pure transverse SAM density can be achieved in the focal plane, and there is no longitudinal SAM density. According to [33], when the electric fields at the central symmetric positions are the complex conjugate of each other in the input plane, the x -component of the tightly focused field is in phase with the y -component, and the z -component and $x(y)$ -component of the tightly focused field are always $\pm\pi/2$ out of phase. Obviously, the electric field of SM-HP-VOF at the central symmetric positions are the complex conjugate of each other, leading to the pure transverse SAM in the focal plane. Meanwhile, the maximum values of the transverse SAM density are also larger than the case of the cylindrical HP-VOF. This proves the advantage of the SM-HP-VOF in achieving pure transverse SAM density.

To further discuss the influence of N on manipulating the transverse SAM density, the total intensity and transverse SAM density of the tightly focused SM-HP-VOF when $(N, m) = (2, 1), (4, 1), (2, 2)$ and $(4, 2)$ are shown in Figure 4. The total intensity of the tightly focused SM-HP-VOF is shown in the first column, and the transverse component S_t , x -component S_x , and y -component S_y of the transverse SAM density are shown in the second to fourth columns. It should be pointed out that the longitudinal SAM density is zero for the tightly focused SM-HP-VOF, which is not shown in Figure 4. From Figure 4 we can see that when $N = 4$, the maximum value of the transverse SAM density is larger than that of the case when $N = 2$. Meanwhile, the transverse SAM density is more concentrated when $N = 4$, as only two peak spots appear for the transverse SAM density. This illustrates that the larger parameter N can concentrate the transverse SAM density and improve the maximum value of it. In addition, the maximum value of S_x is always larger than that of S_y .

In addition to the parameter N , the topological charge m is also an important parameter to modulate the focal intensity and transverse SAM density of the tightly focused SM-HP-VOF. As shown in Figures 4 and 5, the maximum value of the focal intensity is larger when $m = \pm 2$ compared with the case when $m = \pm 1$, and the main spot shrinks when $m = \pm 2$ as well. This means that for the tightly focused SM-HP-VOF, the larger $|m|$ can make the focal spot stronger and more concentrated. It is worth noting that by comparing Figures 4 and 5, the distributions of focal intensity pattern and the transverse SAM density S_t are symmetric about the y axis when N is the same and m is opposite to each other. By comparing S_x and S_y in Figures 4 and 5, it can be found that when N is the same and m is opposite, the distribution of S_x is symmetric to the y axis, while the distribution of S_y is also symmetric to the y axis but with the opposite values. From Figures 4 and 5 we know that the parameters N and m of the SM-HP-VOF can be used in modulating the distribution and symmetry of the intensity and transverse SAM density of the tightly focused SM-HP-VOF.

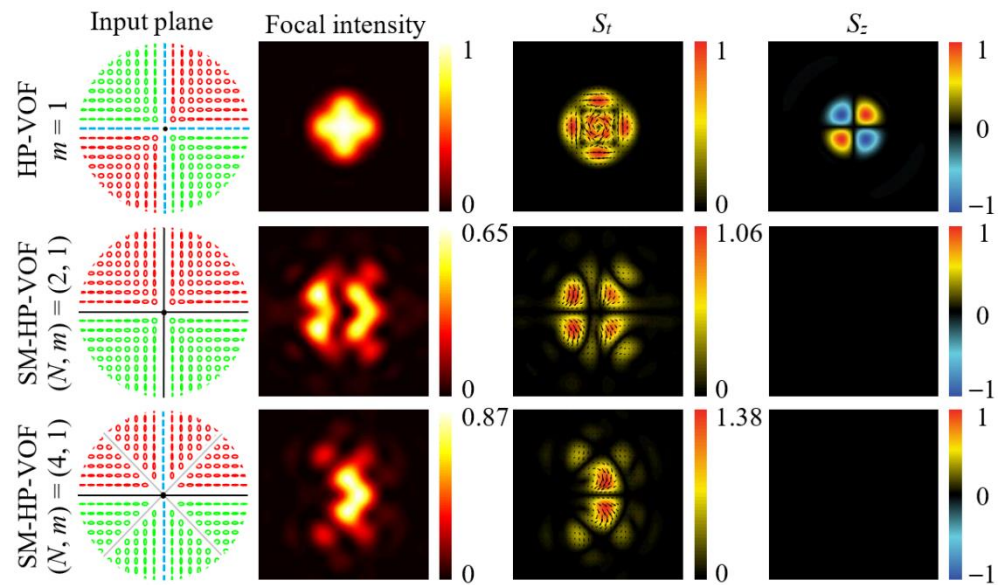


Figure 3. The polarization states of the HP-VOF and the SM-HP-VOF in the input plane are shown in the first column, and the total intensity, transverse SAM density S_t , and longitudinal SAM density S_z in the focal plane are shown in the second to fourth columns. The first row shows the cylindrical HP-VOF when $m = 1$, and the second and third rows show the SM-HP-VOF when $(N, m) = (2, 1)$ and $(4, 1)$, respectively. The blue, red and green polarizations in the first column represent linear, right- and left-handed elliptic (circular) polarizations, respectively. The arrows in the third column indicate the direction of the transverse SAM density. The numerical aperture of the focal lens is $NA = 0.95$, and any picture in the focal plane has a size of $4\lambda \times 4\lambda$, with λ being the wavelength.

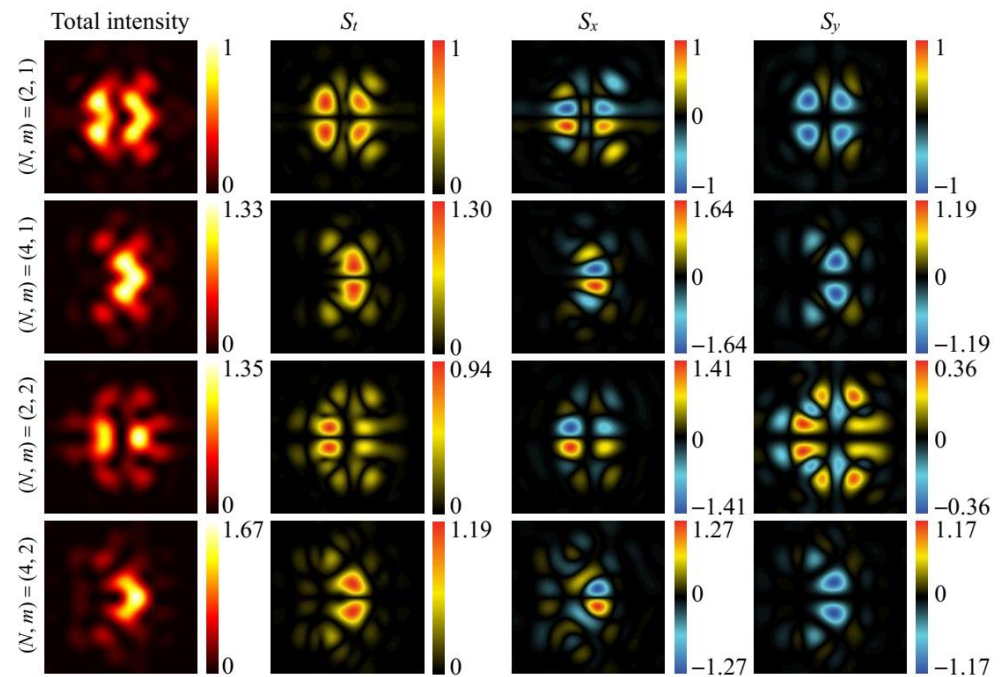


Figure 4. The total intensity and transverse SAM density of the tightly focused SM-HP-VOF when $(N, m) = (2, 1), (4, 1), (2, 2)$ and $(4, 2)$ in the four rows, respectively. The first column shows the total intensity of the tightly focused SM-HP-VOF. For the transverse SAM density, the transverse component S_t , x -component S_x , and y -component S_y are shown in the second to fourth columns, respectively. The numerical aperture of the focal lens is $NA = 0.95$, and any picture in the focal plane has a size of $4\lambda \times 4\lambda$, with λ being the wavelength.

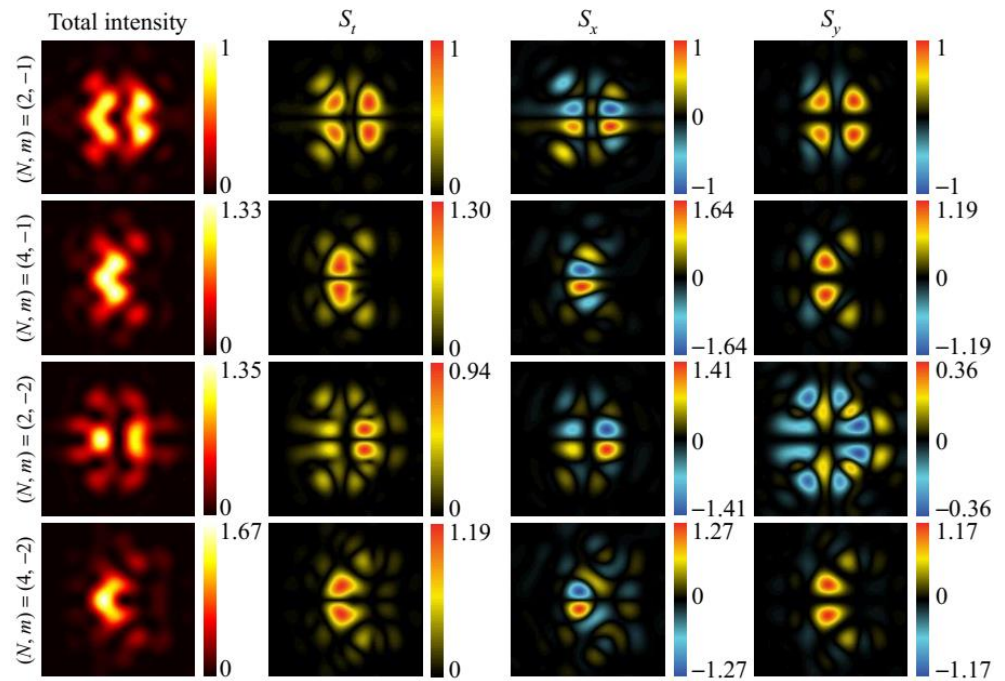


Figure 5. The total intensity and transverse SAM density of the tightly focused SM-HP-VOF when $(N, m) = (2, -1), (4, -1), (2, -2)$ and $(4, -2)$ in the four rows, respectively. The first column shows the total intensity of the tightly focused SM-HP-VOF. For the transverse SAM density, the transverse component S_t , x -component S_x , and y -component S_y are shown in the second to fourth columns, respectively. The numerical aperture of the focal lens is $NA = 0.95$, and any picture in the focal plane has a size of $4\lambda \times 4\lambda$, with λ being the wavelength.

To further enrich the manipulating method of the transverse SAM density with the tightly focused SM-HP-VOF, we added a segmented vortex phase distribution p_n in each sector to the SM-HP-VOF, to help us study the influence of the OAM on the transverse SAM density. As we introduced above, the OAM is related to the space-variant phase distribution, which has been applied in various regions [52–61]. A vortex field with a helical phase of $\exp(-il\varphi)$ can carry an optical OAM of l per photon, where l is the topological charge. The SM-HP-VOF with the phase modulation can be expressed as:

$$\mathbf{E}(\varphi) = \sum_{n=1}^N \mathbf{E}_n(\varphi)e^{ip_n} + \sum_{n=N+1}^{2N} \mathbf{E}_n(\varphi)e^{-ip_n} \tag{8}$$

when $1 \leq n \leq N$ and n is odd, $p_n = l\varphi - (n-1)l\pi/N$, $(n-1)\pi/N \leq \varphi < n\pi/N$. Hence, p_n is limited within a range of $[0, l\pi/N)$, which means that the variation trend of p_n is exactly equivalent to the case of p_1 . When $1 \leq n \leq N$ and n is even, $p_n = ln\pi/N - l\varphi$, $(n-1)\pi/N \leq \varphi < n\pi/N$. Hence, p_n is limited within a range of $[l\pi/N, 0)$, which means that the variation trend of p_n is exactly contrary to the case of p_1 . For the case of the optical field below x axis when $N+1 \leq n \leq 2N$, the attached phase is the complex conjugate of the phase at the central symmetric position. In this way, the segmented vortex phase distribution also is in accord with the symmetry requirement we make.

Figure 6 shows the total intensity and transverse SAM density of the tightly focused SM-HP-VOF with segmented vortex phase modulation when $(N, m) = (4, 1)$. The topological charges of the segmented vortex phases are $l = -2, -1, 0, 1$ and 2 in the first to fifth columns in Figure 6, respectively. When there is no vortex phase distribution and $l = 0$, there are two peak spots in the transverse SAM density pattern. When $|l|$ increases to 2, the two peak spots gradually change to one, and the maximum value increases as well. This means the segmented vortex phase or the segmented OAM distribution can help the SM-HP-VOF

to converge and enhance the transverse SAM density. For opposite topological charges l , the distribution of the focal intensity and the transverse SAM density are both symmetric about the x axis, as shown in the first two rows in Figure 6. However, for the direction of the transverse SAM density S_t , it is not simply symmetric about x axis for opposite l . The directions of the transverse SAM density when $l = 2$ and -2 are both clockwise. This is because the upper peak spot maintains when $l = -2$, while the lower peak spot maintains when $l = 2$.

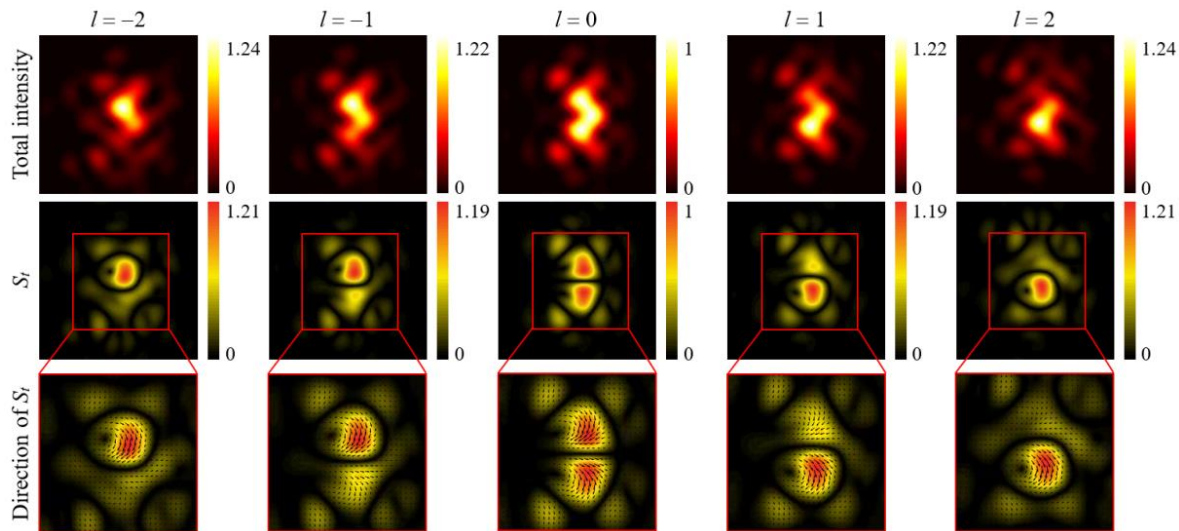


Figure 6. The total intensity and transverse SAM density of the tightly focused SM-HP-VOF with segmented vortex phase modulation when $(N, m) = (4, 1)$. The topological charges of the vortex phases are $l = -2, -1, 0, 1$ and 2 in five columns, respectively. The focal intensity, transverse SAM density S_t and the direction of S_t are given in the three rows, respectively. The numerical aperture of the focal lens is $NA = 0.95$, and any picture in the first two rows has a size of $4\lambda \times 4\lambda$, and any picture in the third row has a size of $2.5\lambda \times 2.5\lambda$.

4. Conclusions

In conclusion, we propose a new kind of SM-HP-VOF, which is designed by dividing the wave front of the optical field into sectors and filling the symmetric polarizations based on the conventional cylindrical HP-VOF. We realized the SM-HP-VOF in an experiment, and the wave fronts were divided into four and eight sectors, respectively. Based on the SM-HP-VOF, pure transverse SAM can be achieved in the focal plane by a focal lens with $NA = 0.95$. By changing the parameters of the SM-HP-VOF, the shape, intensity, and symmetry of the transverse SAM can be manipulated. When a segmented vortex phase is further added to the wave front of the SM-HP-VOF, the transverse SAM becomes more concentrated and stronger. In this way, the OAM can be regarded as a catalyst of manipulating transverse SAM. The newly proposed SM-HP-VOF and the flexibly manipulated transverse SAM can provide new thoughts in studying VOF as well as the transverse SAM, which can be applied in various areas including chip optical circuitry, optical quantum computing, and optical trapping and manipulation.

Author Contributions: Conceptualization, X.-F.S., Y.P. and X.-Z.G.; methodology, Y.P. and X.-Z.G.; software, X.-F.S.; validation, X.-F.S. and Y.P.; formal analysis, X.-F.S. and X.-Z.G.; investigation, X.-F.S., G.-B.Z. and Y.P.; resources, Y.P., X.-Z.G. and Z.-X.M.; writing—original draft preparation, X.-F.S. and Y.P.; writing—review and editing, X.-Z.G. and Z.-X.M.; supervision, Z.-X.M.; funding acquisition, Y.P., X.-Z.G. and Z.-X.M. All authors have read and agreed to the published version of the manuscript.

Funding: This research was funded by National Natural Science Foundation of China (Grant No. 11904199, Grant No. 11974209); Taishan Scholar Project of Shandong Province (Grant No. tsqn201812059).

Institutional Review Board Statement: Not applicable.

Informed Consent Statement: Not applicable.

Data Availability Statement: The data that support the findings of this study are available from the first author and the corresponding author upon reasonable request.

Conflicts of Interest: The authors declare no conflict of interest.

References

1. Zhan, Q. Cylindrical vector beams: From mathematical concepts to applications. *Adv. Opt. Photonics* **2009**, *1*, 1–57. [[CrossRef](#)]
2. Chen, J.; Wan, C.; Zhan, Q. Vectorial optical fields: Recent advances and future prospects. *Sci. Bull.* **2018**, *63*, 54–74. [[CrossRef](#)]
3. Paterson, L.; MacDonald, M.P.; Arlt, J.; Sibbett, W.; Bryant, P.; Dholakia, K. Controlled rotation of optically trapped microscopic particles. *Science* **2001**, *292*, 912–914. [[CrossRef](#)] [[PubMed](#)]
4. Wang, X.-L.; Chen, J.; Li, Y.; Ding, J.; Guo, C.; Wang, H.-T. Optical orbital angular momentum from the curl of polarization. *Phys. Rev. Lett.* **2010**, *105*, 253602. [[CrossRef](#)] [[PubMed](#)]
5. Dorn, R.; Quabis, S.; Leuchs, G. Sharper focus for a radially polarized light beam. *Phys. Rev. Lett.* **2003**, *91*, 233901. [[CrossRef](#)]
6. Wang, H.; Shi, L.; Lukyanchuk, B.; Sheppard, C.; Chong, C.T. Creation of a needle of longitudinally polarized light in vacuum using binary optics. *Nat. Photonics* **2008**, *2*, 501–505. [[CrossRef](#)]
7. Pan, Y.; Gao, X.Z.; Cai, M.Q.; Zhang, G.L.; Li, Y.; Tu, C.; Wang, H.T. Fractal vector optical fields. *Opt. Lett.* **2016**, *41*, 3161–3164. [[CrossRef](#)]
8. Hu, H.; Gan, Q.; Zhan, Q. Generation of a nondiffracting superchiral optical needle for circular dichroism imaging of sparse subdiffraction objects. *Phys. Rev. Lett.* **2019**, *122*, 223901. [[CrossRef](#)]
9. Gabriel, C.; Aiello, A.; Zhong, W.; Euser, T.G.; Joly, N.Y.; Banzer, P.; Fortsch, M.; Elser, D.; Andersen, U.L.; Marquardt, C. Entangling different degrees of freedom by quadrature squeezing cylindrically polarized modes. *Phys. Rev. Lett.* **2011**, *106*, 060502. [[CrossRef](#)]
10. Fickler, R.; Lapkiewicz, R.; Plick, W.N.; Krenn, M.; Schaeff, C.; Ramelow, S.; Zeilinger, A. Quantum entanglement of high angular momenta. *Science* **2012**, *338*, 640–643. [[CrossRef](#)]
11. Daloi, N.; Dey, T.N. Vector beam polarization rotation control using resonant magneto optics. *Opt. Express* **2022**, *30*, 21894–21905. [[CrossRef](#)] [[PubMed](#)]
12. Liu, M.; Lei, Y.Z.; Yu, L.; Fang, X.; Ma, Y.; Liu, L.; Zheng, J.; Gao, P. Super-resolution optical microscopy using cylindrical vector beams. *Nanophotonics* **2022**, *11*, 3395–3420. [[CrossRef](#)]
13. Zhao, N.; Li, X.; Li, G.; Kahn, J.M. Capacity limits of spatially multiplexed free-space communication. *Nat. Photonics* **2015**, *9*, 822–826. [[CrossRef](#)]
14. Gao, X.-Z.; Pan, Y.; Wang, D.; Li, Y.; Tu, C.; Wang, H.-T. Vector optical fields broken in the spatial frequency domain. *Phys. Rev. A* **2016**, *93*, 033834. [[CrossRef](#)]
15. Devlin, R.C.; Ambrosio, A.; Rubin, N.A.; Mueller, J.P.B.; Capasso, F. Arbitrary spin-to-orbital angular momentum conversion of light. *Science* **2017**, *358*, 896–900. [[CrossRef](#)] [[PubMed](#)]
16. Wang, X.-L.; Li, Y.; Chen, J.; Guo, C.-S.; Ding, J.; Wang, H.-T. A new type of vector fields with hybrid states of polarization. *Opt. Express* **2010**, *18*, 10786–10795. [[CrossRef](#)]
17. Lerman, G.M.; Stern, L.; Levy, U. Generation and tight focusing of hybridly polarized vector beams. *Opt. Express* **2010**, *18*, 27650–27657. [[CrossRef](#)] [[PubMed](#)]
18. Colas, D.; Dominici, L.; Donati, S.; Pervishko, A.A.; Liew, T.C.H.; Shelykh, I.A.; Ballarini, D.; De Giorgi, M.; Bramati, A.; Gigli, G.; et al. Polarization shaping of Poincaré beams by polariton oscillations. *Light-Sci. Appl.* **2015**, *4*, e350. [[CrossRef](#)]
19. Shu, W.; Ling, X.; Fu, X.; Liu, Y.; Ke, Y.; Luo, H. Polarization evolution of vector beams generated by q -plates. *Photonics Res.* **2017**, *5*, 64–72. [[CrossRef](#)]
20. Gao, X.-Z.; Wang, M.-S.; Zhao, J.-H.; Zhao, P.-C.; Zhang, X.; Pan, Y.; Li, Y.; Tu, C.; Wang, H.-T. Generation and Tunable Focal Shift of the Hybridly Polarized Vector Optical Fields with Parabolic Symmetry. *Chin. Phys. Lett.* **2020**, *37*, 124201. [[CrossRef](#)]
21. Yang, H.W.; Pan, J.; Zhang, S.; Zhu, W.; Zhang, L.; Zheng, H.; Zhong, Y.; Yu, J.; Chen, Z. Steering Nonlinear Twisted Valley Photons of Monolayer WS_2 by Vector Beams. *Nano Lett.* **2021**, *21*, 7261–7269. [[CrossRef](#)] [[PubMed](#)]
22. Zhao, J.-H.; Pan, Y.; Gao, X.-Z.; Ma, R.; Man, Z.-X.; Ren, Z.-C.; Tu, C.; Li, Y.; Wang, H.-T. Five-dimensional Poincaré sphere system for representing azimuthally varying vector optical fields. *Phys. Rev. A* **2022**, *106*, 023506. [[CrossRef](#)]
23. Bliokh, K.Y.; Bekshaev, A.Y.; Nori, F. Extraordinary momentum and spin in evanescent waves. *Nat. Commun.* **2014**, *5*, 3300. [[CrossRef](#)] [[PubMed](#)]
24. Aiello, A.; Banzer, P.; Neugebauer, M.; Leuchs, G. From transverse angular momentum to photonic wheels. *Nat. Photonics* **2015**, *9*, 789–795. [[CrossRef](#)]
25. Zhu, W.; Shvedov, V.; She, W.; Krolikowski, W. Transverse spin angular momentum of tightly focused full Poincaré beams. *Opt. Express* **2015**, *23*, 34029–34041. [[CrossRef](#)]
26. Li, M.; Yan, S.; Yao, B.; Liang, Y.; Zhang, P. Spinning and orbiting motion of particles in vortex beams with circular or radial polarizations. *Opt. Express* **2016**, *24*, 20604–20612. [[CrossRef](#)]

27. Chen, J.; Wan, C.; Kong, L.; Zhan, Q. Experimental generation of complex optical fields for diffraction limited optical focus with purely transverse spin angular momentum. *Opt. Express* **2017**, *25*, 8966–8974. [[CrossRef](#)]
28. Li, M.; Yan, S.; Liang, Y.; Zhang, P.; Yao, B. Transverse spinning of particles in highly focused vector vortex beams. *Phys. Rev. A* **2017**, *95*, 053802. [[CrossRef](#)]
29. Chen, J.; Wan, C.; Kong, L.; Zhan, Q. Tightly focused optical field with controllable photonic spin orientation. *Opt. Express* **2017**, *25*, 19517–19528. [[CrossRef](#)]
30. Neugebauer, M.; Eismann, J.S.; Bauer, T.; Banzer, P. Magnetic and Electric Transverse Spin Density of Spatially Confined Light. *Phys. Rev. X* **2018**, *8*, 021042. [[CrossRef](#)]
31. Han, L.; Liu, S.; Li, P.; Cheng, H.; Zhao, J. Catalyst like effect of orbital angular momentum on the conversion of transverse to three-dimensional spin states within tightly focused radially polarized beams. *Phys. Rev. A* **2018**, *97*, 053802. [[CrossRef](#)]
32. Pan, Y.; Gao, X.-Z.; Zhang, G.-L.; Li, Y.; Tu, C.; Wang, H.-T. Spin angular momentum density and transverse energy flow of tightly focused kaleidoscope-structured vector optical fields. *APL Photonics* **2019**, *4*, 096102. [[CrossRef](#)]
33. Gao, X.-Z.; Zhao, J.-H.; Wang, M.-S.; Liu, J.-J.; Zhang, G.-B.; Pan, Y. Bipolar-variant spin angular momentum and its evolution in a tight focusing process. *Phys. Rev. A* **2020**, *102*, 063514. [[CrossRef](#)]
34. Qin, Y.; Ji, B.; Song, X.; Lin, J. Disclosing transverse spin angular momentum of surface plasmon polaritons through independent spatiotemporal imaging of its in-plane and out-of-plane electric field components. *Photonics Res.* **2020**, *8*, 1042–1048. [[CrossRef](#)]
35. Eismann, J.S.; Nicholls, L.H.; Alonso, M.A.; Banzer, P.; Rodriguez-Fortuno, F.J.; Zayats, A.V.; Nori, F.; Bliokh, K.Y. Transverse spinning of unpolarized light. *Nat. Photonics* **2021**, *15*, 156–161. [[CrossRef](#)]
36. Gao, X.-Z.; Zhao, J.-H.; Zhao, P.-C.; Sun, X.-F.; Yang, F.; Liu, J.-J.; Pan, Y. Purely transverse spin angular momentum modulated by the singularity phase. *J. Opt.* **2021**, *23*, 115603. [[CrossRef](#)]
37. Zhang, X.; Shen, B.; Zhu, Z.; Rui, G.; He, J.; Cui, Y.; Gu, B. Understanding of transverse spin angular momentum in tightly focused linearly polarized vortex beams. *Opt. Express* **2022**, *30*, 5121–5130. [[CrossRef](#)]
38. Ma, Y.; Zhao, H.; Liu, N.; Gao, Z.; Mohajerani, S.S.; Xiao, L.; Hone, J.; Feng, L.; Strauf, S. On-chip spin-orbit locking of quantum emitters in 2D materials for chiral emission. *Optica* **2022**, *9*, 953–958. [[CrossRef](#)]
39. Meng, X.; Wan, C.; Zhan, Q. Transversely oriented cylindrically polarized optical fields. *Opt. Express* **2022**, *30*, 14897–14909. [[CrossRef](#)]
40. Gu, B.; Wen, B.; Rui, G.; Xue, Y.; Zhan, Q.; Cui, Y. Varying polarization and spin angular momentum flux of radially polarized beams by anisotropic Kerr media. *Opt. Lett.* **2016**, *41*, 1566–1569. [[CrossRef](#)]
41. Chen, R.-P.; Chew, K.-H.; Dai, C.-Q.; Zhou, G. Optical spin-to-orbital angular momentum conversion in the near field of a highly nonparaxial optical field with hybrid states of polarization. *Phys. Rev. A* **2017**, *96*, 053862. [[CrossRef](#)]
42. Chen, R.-P.; Gao, T.-Y.; Chew, K.-H.; Dai, C.-Q.; Zhou, G.-Q.; He, S.-L. Near-field characteristics of highly non-paraxial subwavelength optical fields with hybrid states of polarization. *Chin. Phys. B* **2017**, *26*, 104202. [[CrossRef](#)]
43. Li, P.; Guo, X.; Qi, S.; Han, L.; Zhang, Y.; Liu, S.; Li, Y.; Zhao, J. Creation of independently controllable multiple focal spots from segmented Pancharatnam-Berry phases. *Sci. Rep.* **2018**, *8*, 9831. [[CrossRef](#)] [[PubMed](#)]
44. Guan, Y.; Zhong, L.-X.; Qian, C.-Y.; Chen, R.-P. Three-Dimensional Optical Spin Angular Momentum Flux of a Vector Beam with Radially-Variant Polarization in Near Field. *Appl. Sci.* **2019**, *9*, 960. [[CrossRef](#)]
45. Kotlyar, V.V.; Stafeev, S.S.; Kozlova, E.S.; Nalimov, A.G. Spin-Orbital Conversion of a Strongly Focused Light Wave with High-Order Cylindrical-Circular Polarization. *Sensors* **2021**, *21*, 6424. [[CrossRef](#)]
46. Chen, H.; Hao, J.; Zhang, B.-F.; Xu, J.; Ding, J.; Wang, H.-T. Generation of vector beam with space-variant distribution of both polarization and phase. *Opt. Lett.* **2011**, *36*, 3179–3181. [[CrossRef](#)]
47. Richards, B.; Wolf, E. Electromagnetic diffraction in optical systems II. Structure of the image field in an aplanatic system. *Proc. Roy. Soc. A* **1959**, *253*, 358–379.
48. Youngworth, K.S.; Brown, T.G. Focusing of high numerical aperture cylindrical-vector beams. *Opt. Express* **2000**, *7*, 77–87. [[CrossRef](#)]
49. Berry, M.V. Paraxial beams of spinning light. *Proc. SPIE* **1998**, *3487*, 6–11.
50. Cameron, R.P.; Barnett, S.M. Electric-magnetic symmetry and Noether's theorem. *New J. Phys.* **2012**, *14*, 123019. [[CrossRef](#)]
51. Bliokh, K.Y.; Bekshaev, A.Y.; Nori, F. Dual electromagnetism: Helicity, spin, momentum and angular momentum. *New J. Phys.* **2013**, *15*, 033026. [[CrossRef](#)]
52. Yao, A.M.; Padgett, M.J. Orbital angular momentum: Origins, behavior and applications. *Adv. Opt. Photonics* **2011**, *3*, 161–204. [[CrossRef](#)]
53. Wang, J. Advances in communications using optical vortices. *Photonics Res.* **2016**, *4*, B14–B28. [[CrossRef](#)]
54. Rubinsztein-Dunlop, H.; Forbes, A.; Berry, M.V.; Dennis, M.R.; Andrews, D.L.; Mansuripur, M.; Denz, C.; Alpmann, C.; Banzer, P.; Bauer, T.; et al. Roadmap on structured light. *J. Opt.* **2017**, *19*, 013001. [[CrossRef](#)]
55. Vitullo, D.L.P.; Leary, C.C.; Gregg, P.; Smith, R.A.; Reddy, D.V.; Ramachandran, S.; Raymer, M.G. Observation of Interaction of Spin and Intrinsic Orbital Angular Momentum of Light. *Phys. Rev. Lett.* **2017**, *118*, 083601. [[CrossRef](#)] [[PubMed](#)]
56. Shen, Y.; Wang, X.; Xie, Z.; Min, C.; Fu, X.; Liu, Q.; Gong, M.; Yuan, X. Optical vortices 30 years on: OAM manipulation from topological charge to multiple singularities. *Light Sci. Appl.* **2019**, *8*, 90. [[CrossRef](#)]
57. Fang, X.; Ren, H.; Gu, M. Orbital angular momentum holography for high-security encryption. *Nat. Photonics* **2020**, *14*, 102. [[CrossRef](#)]

58. Chong, A.; Wan, C.; Chen, J.; Zhan, Q. Generation of spatiotemporal optical vortices with controllable transverse orbital angular momentum. *Nat. Photonics* **2020**, *14*, 350. [[CrossRef](#)]
59. Bliokh, K.Y. Spatiotemporal Vortex Pulses: Angular Momenta and Spin-Orbit Interaction. *Phys. Rev. Lett.* **2021**, *126*, 243601. [[CrossRef](#)]
60. Wang, J.; Liu, J.; Li, S.; Zhao, Y.; Du, J.; Zhu, L. Orbital angular momentum and beyond in free-space optical communications. *Nanophotonics* **2021**, *11*, 645–680. [[CrossRef](#)]
61. Forbes, A.; de Oliveira, M.; Dennis, M.R. Structured light. *Nat. Photonics* **2021**, *15*, 253–262. [[CrossRef](#)]